JOURNAL OF SOLID STATE CHEMISTRY **122,** 416–427 (1996)
ARTICLE NO. 0135

Structure and Magnetism in $AB_{10}O_{15+x}$ (A = Sr, Ba; B = V, Cr; x = 0, ~1): Evidence for Geometric Frustration[1]

Guo Liu and J. E. Greedan

Brockhouse Institute for Materials Research, McMaster University, Hamilton, Ontario L8S 4M1, Canada

Received July 10, 1995; accepted January 11, 1996

Some members of the series $AB_{10}O_{15+x}$, A = Sr, Ba, B = V, Cr, x = 0 and ~1, have been studied and are found to possess unusual magnetic properties which can be traced to geometric frustration of the B-site magnetic sublattice. These compounds crystallize in *Cmca* and the structure can be described as a hexagonal close packing of alternating AO_7 and O_8 layers with the B ions occupying 5/8 of the octahedral sites. The presence of A^{2+} ions in the close packed AO_7 layers directs the pattern of B-site occupation and octahedral sites near the A^{2+} ions are forbidden. The resulting B sublattice consists of B_{10} clusters of edge-sharing, distorted tetrahedra connected by corner-sharing to adjacent clusters to form a three-dimensional network. $SrV_{10}O_{15}$ shows a sharp susceptibility maximum at 50 K and powder neutron diffraction provides evidence for long range magnetic order. In contrast, $BaCr_{10}O_{15}$ shows only a broad susceptibility maximum at 25 K but a field-cooled–zero-field cooled divergence at 30 K, i.e., spin glass-like behavior. Neutron diffraction detects only short range (SRO) antiferromagnetic (AF) order in the form of diffuse scattering consistent with a correlation length corresponding to the distance between nearest neighbors. The AFSRO sets in below 180 K and surprisingly, ferromagnetic SRO appears below 8 K. The properties of $BaCr_{10}O_{15}$ and $BaCr_{10}O_{15+x}$ are compared to Cr_2O_3 which is also based on an hcp lattice with nearly the same octahedral site occupation rate, 2/3 versus 5/8, and which shows no evidence of frustration.

INTRODUCTION

Metal oxides of the composition $AB_{10}O_{15}$ where A = Sr or Ba and B = V or Cr have been reported fairly recently (1, 2). To date only small single crystals, prepared from high temperature melts, are available and structures have been determined from single crystal X-ray diffraction data. In some cases the report of the structural details is incomplete by present conventions. One member of this series, $BaV_{10}O_{15}$, has been encountered quite recently as an intermediate phase which forms during the reduction of $Ba_2V_2O_7$ under hydrogen to form $BaVO_{2.8}$ (3).

As will be shown later, close compositional and structural relationships exist with the well-studied binary oxides V_2O_3 and Cr_2O_3. As of yet, no physical properties have been reported.

In the following study procedures are described for the preparation of bulk, polycrystalline samples, structure refinements are reported from powder neutron and single crystal X-ray data, and magnetic and electrical properties are presented with particular attention to $SrV_{10}O_{15}$ and $BaCr_{10}O_{15}$. An attempt is made to correlate the unusual magnetic behavior with features of the crystal structure, in particular the topology of the B-site sublattice which presents the potential for geometrical frustration. It will be shown that in the cases of $BaCr_{10}O_{15}$ and $BaCr_{10}O_{15+x}$ there is strong evidence for frustration.

EXPERIMENTAL

Synthesis of Polycrystalline Materials

$BaM_{10}O_{15}$(M = Cr, V). Stoichiometric mixtures of $BaCO_3$ and V_2O_3, or $BaCO_3$ and appropriate amounts of V_2O_3 and Cr_2O_3, were mixed and ground intimately with acetone, dried, and pelleted. Samples, typically 1–2 g, were contained in alumina boats and reduced in H_2 in a tubular furnace at 1300–1350°C for 24 h. Regrinding and reheating were sometimes necessary depending on the sample mass and the degree of mixing. The purity was checked by powder X-ray diffraction.

Purer samples could be obtained by heating the H_2 reduction product contained in Mo crucibles at 1600°C in an induction furnace for 3 to 10 h. However, for $BaV_{10}O_{15}$ and for $SrV_{10}O_{15}$, especially the former, the hydrogen-reduced and the 1600°C-treated specimens had different magnetic properties.

[1] See NAPS Document 05291 for 91 pages of supplementary materials. Order from ASIS/NAPS, Microfiche Publications, P.O. Box 3513, Grand Center Station, New York, NY 10163-3513. Remit in advance $4.00 for microfiche copy or for photocopy, $7.75 for up to 20 pages plus $0.30 for each additional page. All orders must be prepaid. Institutions and organizations may order by purchase order. However, there is a billing and handling charge for this service of $15.00. Foreign orders add $4.50 for postage and handling, for the first 20 pages, $1.00 for each additional 10 pages of material, and $1.50 for postage of any microfiche orders.

0022-4596/96 $18.00

V_2O_3 was a better precursor than V_2O_5 because when the latter was used the product pellets expanded and broke apart due to the release of large amounts of water during H_2 reduction and as a result it was difficult to make the $BaM_{10}O_{15}$ phase pure.

$SrV_{10}O_{15}$. It was not possible to prepare polycrystalline $SrCr_{10}O_{15}$ by the methods outlined for the Ba-based compounds, only $SrV_{10}O_{15}$ could be synthesized. The procedures are the same as with the $BaM_{10}O_{15}$ systems except that the starting materials were mixtures of SrV_2O_6 and appropriate amounts of V_2O_3 and/or Cr_2O_3. When $SrCO_3$ instead of SrV_2O_6 was used, intimate mixing was hard to achieve because of the small volume of $SrCO_3$ required.

$AM_{10}O_{15+x}$(A = Sr, Ba; M = Cr, V). $AM_{10}O_{15}$ pellets from the hydrogen reduction and V_2O_5 powder at a 2:1 molar ratio were contained in separate open quartz tubes, which were then sealed together in an evacuated quartz tube, and heated at 2°/min to 800°C for 1 to 2 days. The V_2O_5 powder was used as an oxygen source. The product always contained V_2O_3 or Cr_2O_3 impurities, and thus no chemical analysis was performed. The conversion of $AM_{10}O_{15}$ into $AM_{10}O_{15+x}$ was evidenced by the weight gain of the specimens and significant changes in unit cell parameters (Table 4).

Thermal Analysis—$SrV_{10}O_{15}$

A thermal gravimetric weight gain analysis was carried out on $SrV_{10}O_{15}$ using a Netzsch STA409 thermal analyzer in an atmosphere of flowing O_2 at 450°C. A weight gain of 20.4% was observed compared with an expected value of 21.0%, indicating a composition only slightly oxidized relative to the ideal composition.

Crystal Growth of $BaV_{10}O_{15}$

The melting point of $BaV_{10}O_{15}$ was found to be about 1840°C by observing the melting of $BaV_{10}O_{15}$ pellets in an open Mo crucible while heating in an induction furnace. Pellets of the sample were then sealed in a Mo crucible under 0.5 atm argon, heated slowly to about 1920°C, and cooled by gradually reducing the power level of the induction furance. Black, shiny crystals were found in the melt.

All the $AM_{10}O_{15}$-type compounds were found to be volatile even at 1600°C. Occasionally, crystals could be found even after powder specimens were heated in vacuum in Mo crucibles covered with Mo lids (but not sealed) at 1600°C for 3–10 h. Prolonged heating in sealed tubes at temperatures well above the melting points sometimes led to the breaking of the crucibles due to high vapor pressures.

Powder X-Ray and Neutron Diffraction

Polycrystalline specimens and pulverized crystals were examined using a 100 mm diameter Guinier–Hägg camera with Cu$K\alpha_1$ radiation and a silicon internal standard. Procedures for powder X-ray (3) have been described previously. Ambient and low temperature neutron data were collected on the DUALSPEC instrument at the Chalk River Nuclear Laboratory using 1.4993(3) and 2.5042(6) Å neutrons, respectively, and at the McMaster Nuclear Reactor with 1.3920 Å neutrons.

Data processing was effected on an IBM-compatible 80486 personal computer. Rietveld refinement was done using the program FULLPROF due to Rodríguez-Carvajal (4), PC version 2.5 (April 1994) and based on the code of DBW3.2S by Wiles, Sakthivel, and Young and described in (5).

Single Crystal X-Ray Diffraction of $BaV_{10}O_{15}$

A black crystal was mounted on the tip of a glass fiber using epoxy cement. Data were collected on a Siemens P3 four-circle diffractometer with Ag$K\alpha$ radiation. Three standard reflections were collected every 97 reflections. Data reduction and structure solution were also performed on an 80486 PC using the Siemens SHELXTL PC (release 4.2, 1991) software package. Absorption corrections were applied with azimuthally scanned data using the program XEMP. Systematic extinctions were consistent with the space groups *Cmca* (No. 64, centrosymmetric) and *Aba*2 (No. 41, noncentrosymmetric). Intensity statistics suggested the most likely space group to be *Cmca.* Ba and most of the vanadium atoms were located by direct methods, and the rest of the atoms by difference Fourier. Scattering factors of neutral atoms have been employed. The structure was refined by full-matrix least-squares on F^2 using the program SHELXL, part of the SHELXL-92 test version (6). The details are presented in Tables 1 and 2.

Magnetic and Electrical Measurements

Magnetic moments for polycrystalline samples were obtained using a Quantum Design SQUID magnetometer in the temperature range from 5 to 300 K. Diamagnetic corrections were applied according to Selwood (7). Electrical resistivities were obtained on sintered pellets by the four-probe method.

RESULTS AND DISCUSSION

Description of the Crystal Structure

The crystal symmetry is orthorhombic, *Cmca,* with $Z = 4$ and the structure has been described from several perspectives in previous reports (1, 2). Features most relevant to an understanding of the physical properties are shown in Figs. 1–4. First, the structure can be described as hexagonal close packing of layers of composition AO_7 alternating with those of composition O_8 with B atoms occupying 5/8 of the octahedral sites. This layering is seen

TABLE 1
Crystal Data and Structure Refinement for $BaV_{10}O_{15}$

Empirical formula	$Ba_4V_{40}O_{60}$
Formula weight	3546.96
Temperature	293(2) K
Wavelength	0.56086 Å
Crystal system	Orthorhombic
Space group	*Cmca*
Unit cell dimensions	$a = 11.584(4)$ Å $\alpha = 90°$
	$b = 9.946(3)$ Å $\beta = 90°$
	$c = 9.383(4)$ Å $\gamma = 90°$
Volume	1081.1(7) Å^3
Z	1
Density (calculated)	5.448 Mg/m^3
Absorption coefficient	6.136 mm^{-1}
$F(000)$	1624
Crystal size	$0.19 \times 0.08 \times 0.09$ mm^3
θ range for data collection	2.73° to 30.08°
Index ranges	$0 \le h \le 20$, $0 \le k \le 17$, $-16 \le l \le 0$
Reflections collected	1657
Independent reflections	1657 [R(int) = 0.0000]
Refinement method	Full-matrix least-squares on F^2
Data/restraints/parameters	1657/0/68
Goodness-of-fit on F^2	0.901
Final R indices [$I > 2\sigma(I)$]	$R1 = 0.0540$, w$R2 = 0.1261$
R indices (all data)	$R1 = 0.0905$, w$R2 = 0.1393$
Largest diff. peak and hole	3.305 and −1.934 e Å^{-3}

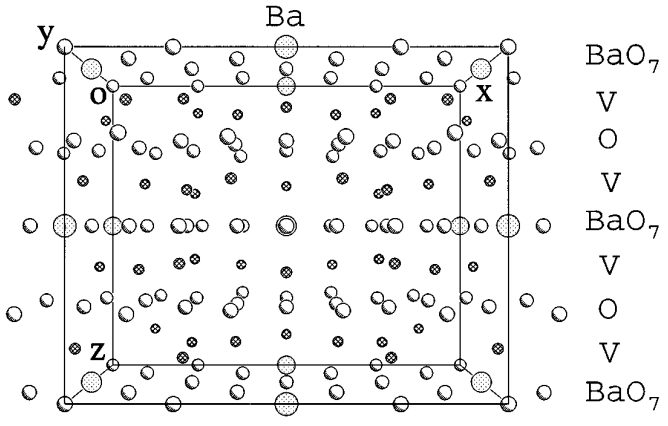

FIG. 1. The unit cell of $BaV_{10}O_{15}$ projected down the b axis to show the layered structure.

most clearly in Fig. 1. Of course the A^{2+} ions are not randomly distributed within the AO_7 layers but order due to electrostatic forces as seen from the view of a single layer in Fig. 2. An important implication of A^{2+} order in the AO_7 layers is that the occupation of the available octahedral sites will be restricted to a specific pattern which avoids proximity to the A^{2+} sites. A part of the B-site sublattice viewed along (001) is shown in Fig. 3. The pattern within a single layer is seen to be based on B_5 clusters which are comprised of three edge-sharing triangles which are then connected by a single B–B link to adjacent clusters. In fact the pattern of B-site occupation in three dimensions features double layers of B_{10} clusters clearly seen in Fig. 3. Each B atom is connected to its nearest intracluster neighbors by a triangular linkage as well. The B_{10} double layers are stacked along the c axis in an $ABAB\ldots$ sequence and the intercluster connection is by a two-atom B–B interaction of the same geometry as the intralayer connection. It is clear from the above description that all nearest neighbor B–B interactions, intracluster or intercluster, involve triangular B–B–B pathways and thus present the potential for magnetic frustration if antiferromagnetic interactions predominate. Overall, the B sublattice is three-dimensional in its topology as the intra- and intercluster B–B distances are very similar which will be demonstrated later in Tables 3 and 6. Figure 4 shows three layers, AO_7, B, and O_8, showing all of the atoms in a polyhedral representation which emphasizes the B–O bonding interactions which involve edge-sharing B–O_6 octahedra.

TABLE 2
Atomic Coordinates ($\times 10^4$) and Equivalent Isotropic Displacement Parameters (Å^2 $\times$ 10^3) for $BaV_{10}O_{15}$

	x	y	z	U(eq)[a]
Ba	0	5000	0	14(1)
V(1)	5000	6769(1)	1378(1)	7(1)
V(2)	3714(1)	4106(1)	1370(1)	9(1)
V(3)	−2459(1)	6709(1)	1113(1)	9(1)
O(1)	−2559(5)	5000	0	8(1)
O(2)	1202(3)	2452(4)	6(5)	9(1)
O(3)	2500	3256(5)	2500	7(1)
O(4)	6297(3)	5883(3)	2445(4)	8(1)
O(5)	5000	3438(5)	2484(7)	7(1)
O(6)	5000	5000	0	8(1)

[a] U(eq) is defined as one third of the trace of the orthogonalized U_{ij} tensor.

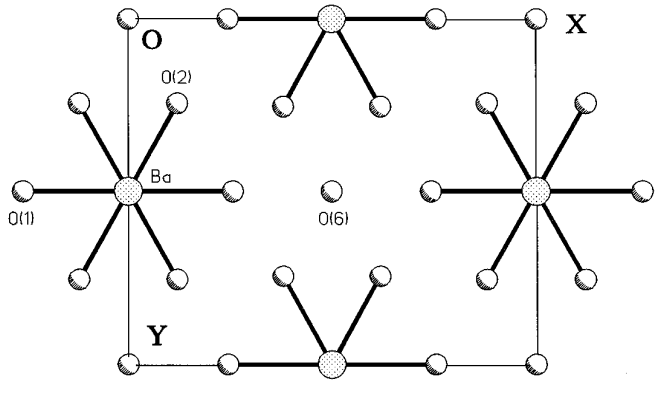

FIG. 2. Ordering of the Ba atoms within the BaO_7 layers in $BaV_{10}O_{15}$ or $BaCr_{10}O_{15}$.

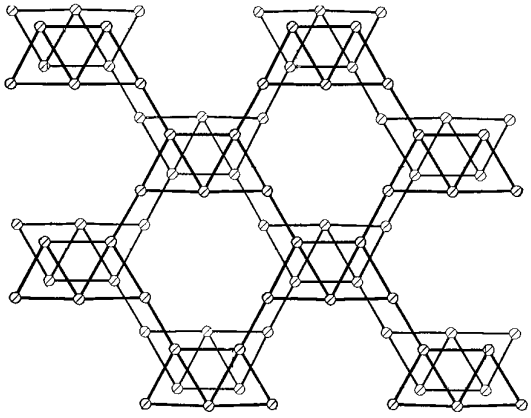

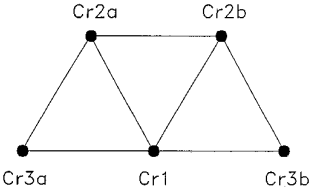

FIG. 3. Part of the B sublattice in $AB_{10}O_{15}$ showing one double layer of B_{10} clusters. There are two such double layers per unit cell which are stacked $ABAB\ldots$ Also shown is one Cr_5 unit with atom labeling relevant to Table 6.

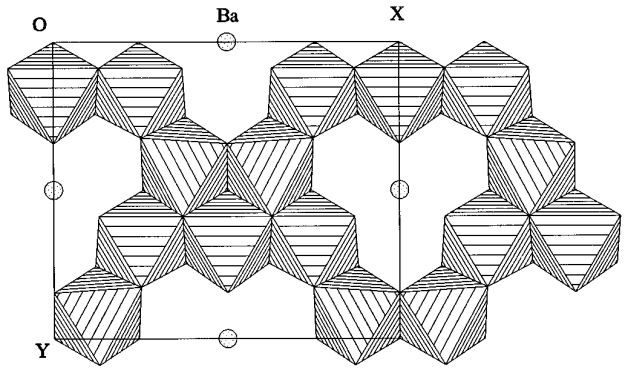

FIG. 4. Three layers, BaO_7, B_{10}, and O_8, in $BaV_{10}O_{15}$ in a polyhedral representation.

Single Crystal Refinement of $BaV_{10}O_{15}$

In the previous study of this compound no e.s.d.'s were reported for any refined structural or thermal parameters (1). The results obtained in this study are shown in Tables 2 and 3 and with regard to bond distances are in good agreement with the previous report although a statistical comparison cannot be made.

Neutron Powder Refinements of $BaCr_{10}O_{15}$ and $BaCr_{10}O_{15+x}$

Although the structure of $BaCr_{10}O_{15}$ has been reported from X-ray studies on small crystals it was considered necessary to establish that the polycrystalline material studied here by bulk susceptibility and neutron diffraction methods was the same. In addition it was also of importance to investigate the structural differences between $BaCr_{10}O_{15}$ and the oxidized form, $BaCr_{10}O_{15+x}$. Powder neutron diffraction is an ideal technique for such comparisons. Figure 5 displays the raw data and the Rietveld fit for $BaCr_{10}O_{15}$. Refinement results for both materials are shown in Tables 4 and 5 and selected bond distances are collected in Table 6. A set of Cr–Cr distances and angles is included as these have relevance for the magnetic properties. These results agree well with the previous report (2).

B-Site Order/Disorder

The $AB_{10}O_{15}$ phases are formally mixed valence compounds, $A^{2+}B_2^{2+}B_8^{3+}O_{15}$. In *Cmca* the B site positions are $B(1)$ in $8f$ and $B(2)$ and $B(3)$ in $16g$, that is, the $B(1):B(2):B(3)$ ratios are $2:4:4$. This raises the possibility that the B^{2+}/B^{3+} ions may order over the available positions. Examination of the average B–O distances, Tables 3 and 6 and Ref. (1), suggest that in $SrV_{10}O_{15}$ and $BaV_{10}O_{15}$, the distribution of V^{2+} and V^{3+} is random while for $SrCr_{10}O_{15}$ and $BaCr_{10}O_{15}$ there is an indication, both from the original X-ray study and the present neutron

TABLE 3
Selected Bond Distances in $BaV_{10}O_{15}$ (Å)

Ba–O1(×2)	2.964(6)		V2–O1(×1)	2.058(4)	
Ba–O2(×4)	2.891(4)		V2–O2(×1)	2.020(4)	
Ba–O4(×4)	2.963(4)		V2–O3(×1)	1.954(2)	Mean
Ba–O5(×2)	2.826(6)		V2–O4(×1)	2.035(3)	2.027(3)
V1–O2(×2)	2.014(4)		V2–O5(×1)	1.937(4)	
V1–O4(×2)	2.009(4)	Mean	V2–O6(×1)	2.159(1)	
V1–O5(×1)	1.974(5)	2.034(4)	V2–V3(×1)	2.756(1)	
V1–O6(×1)	2.183(1)		V2–V3(×1)	2.864(2)	
V1–V2(×2)	3.038(2)		V2–V3(×1)	2.978(1)	
V1–V2(×2)	3.102(2)		V2–V2(×1)	2.979(2)	
V1–V3(×2)	2.954(1)		V2–V1(×1)	3.038(2)	
V3–O1(×1)	1.998(1)		V2–V1(×1)	3.102(2)	
V3–O2(×1)	1.981(4)	Mean	V3–V3(×1)	2.604(2)	
V3–O2(×1)	2.008(4)	2.026(4)	V3–V3(×1)	2.618(2)	
V3–O3(×1)	2.016(4)		V3–V2(×1)	2.756(1)	
V3–O4(×1)	2.076(4)		V3–V2(×1)	2.864(2)	
V3–O4(×1)	2.077(4)		V3–V1(×1)	2.954(1)	
			V3–V2(×1)	2.987(1)	

Sum of Ionic Radii

V^{2+}–O^{2-}	2.17 Å
V^{3+}–O^{2-}	2.02 Å

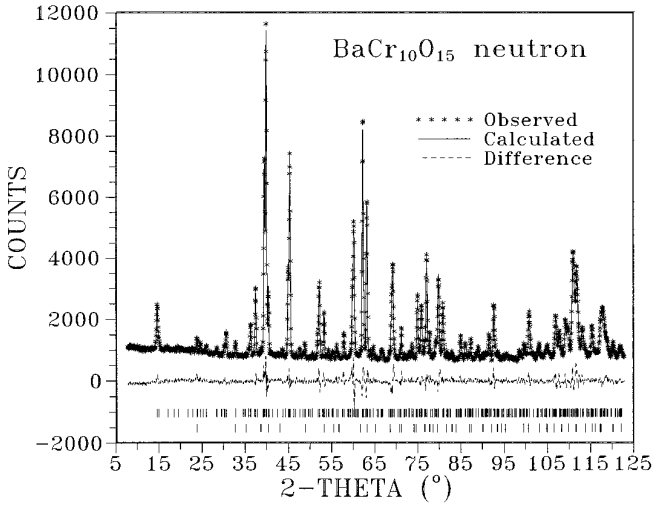

FIG. 5. Rietveld fit of neutron powder diffraction data for $BaCr_{10}O_{15}$. The crosses represent the data, the solid line is the calculated profile and the difference plot is shown below the profile. Vertical tic marks locate the Bragg peak positions for the two phases present, $BaCr_{10}O_{15}$ (top), Cr_2O_3 (bottom).

TABLE 4
Neutron Powder Refinement Conditions for $BaCr_{10}O_{15}$ and $BaCr_{10}O_{15+x}$ in *CmCa*[a]

	$BaCr_{10}O_{15}$	$BaCr_{10}O_{15+x}$
Wavelength (Å)	1.4993(1)	1.4993(1)
	Cell parameters	
a (Å)	11.4537(5)	11.3894(4)
b (Å)	10.0926(5)	10.0040(3)
c (Å)	9.3441(4)	9.2470(3)
V (Å^3)	1080.16(1)	1053.60(1)
2θ range (°)	6.00–120.95	6.00–120.95
Step size	0.05	0.05
Bragg R_B	0.0572	0.0634
Weighted profile R_{wp}	0.0698	0.0754
Profile R_P	0.0526	0.0542
Expected R_E	0.0280	0.0320
Goodness of fit, S	2.49	2.36
Profile points (N)	2211	2209
Parameters refined (P)	55	53
Independent hkl	478	465

$$R_B = \Sigma\,|I_{OBS} - I_{CAL}|$$

$$R_{wp} = \{[\Sigma\, w(Y_{OBS} - Y_{CAL}/c)^2]/\Sigma\, wY^2_{OBS}\}^{1/2}$$

$$R_P = \Sigma\,|Y_{OBS} - Y_{CAL}/c|/\Sigma\, Y_{OBS}$$

$$R_E = [(N - P)/\Sigma\, Y^2_{OBS}]^{1/2}$$

$$s = \frac{R_{wp}}{R_E}$$

[a] Both samples contained a Cr_2O_3 impurity phase. Weight percentages of Cr_2O_3 determined by quantitative two phase refinement are $BaCr_{10}O_{15}$, 10.1(6)% and $BaCr_{10}O_{15+x}$, 20.7(7)%.

TABLE 5
Positional and Thermal Parameters Obtained from Profile Refinement of Neutron Powder Data for $BaCr_{10}O_{15}$ and $BaCr_{10}O_{15+x}$ in *Cmca*

	x	y	z	B (Å^2)
		$BaCr_{10}O_{15}$		
Ba	0.0	0.0	0.5	1.7(4)
Cr1	0.5	0.6786(13)	0.1428(19)	0.4(2)
Cr2	0.3731(11)	0.4137(9)	0.1432(10)	0.4(2)
Cr3	−0.2468(9)	0.6669(9)	0.1150(10)	0.3(2)
O1	−0.2563(7)	0.5	0.0	0.02(16)
O2	0.1275(8)	0.2360(6)	−0.0066(7)	0.5(1)
O3	0.25	0.3208(11)	0.25	0.9(2)
O4	06274(7)	0.5884(7)	0.2456(8)	0.2(1)
O5	0.5	0.3502(10)	0.2615(12)	0.5(2)
O6	0.5	0.5	0.0	0.9(3)
		$BaCr_{10}O_{15+x}$		
Ba	0.0	0.5	0.0	1.9(5)
Cr1	0.5	0.6808(12)	0.1299(18)	−0.6(2)
Cr2	0.3768(11)	0.4149(10)	0.1411(10)	−0.04(17)
Cr3	−0.2402(10)	0.6613(16)	0.1187(15)	1.9(3)
O1	−0.2595(7)	0.5	0.0	−0.3(2)
O2	0.1285(9)	0.2374(6)	−0.0032(8)	0.4(1)
O3	0.25	0.3259(13)	0.25	0.4(2)
O4	0.6230(11)	0.5890(8)	0.2434(7)	0.4(2)
O5	0.5	0.3400(13)	0.2583(12)	0.11(3)
O6	0.5	0.5	0.0	

results, of a partial site preference for Cr^{2+} at the $B(1)$ or $8f$ site. The data also show that the Cr–O distances in the oxidized phase are all equivalent and are consistent with Cr^{3+}. An attempt was made to locate the extra oxygen in $BaCr_{10}O_{15+x}$, but this was not successful. The significant change in Cr–O distances and the unit cell constants indicate clearly that $BaCr_{10}O_{15+x}$, is indeed an oxidized product.

Electrical Properties

A more detailed consideration of electrical transport in these materials will be deferred to a subsequent publication. The results of resistivity measurements on sintered polycrystalline samples are shown in Fig. 6 for $SrV_{10}O_{15}$ and $BaV_{10}O_{15}$. Measurements of polycrystalline $BaCr_{10}O_{15}$ and $BaCr_{10}O_{15+x}$ are not reported due to the two phase nature of the samples but simple two probe measurements on sintered pellets indicated a high room temperature resistance on the order of several kilo-ohms.

Magnetic Susceptibility

The results of dc susceptibility measurements for $SrV_{10}O_{15}$, $BaCr_{10}O_{15}$, and $BaCr_{10}O_{15+x}$ are displayed in Figs. 7 and 8. Results for $BaV_{10}O_{15}$ are not shown as the properties were a very strong function of the preparation

TABLE 6
Selected Bond Distances in $BaCr_{10}O_{15}$ and $BaCr_{10}O_{15+x}$ (Å)

	$BaCr_{10}O_{15}$		$BaCr_{10}O_{15+x}$	
Ba–O1(×2)	2.936(8)		2.956(8)	
Ba–O2(×4)	3.039(7)		3.007(7)	
Ba–O4(×4)	2.929(8)		2.896(8)	
Ba–O5(×2)	2.693(11)		2.749(12)	
Cr1–O2(×2)	2.102(15)		1.994(14)	
Cr1–O4(×2)	1.970(13)	Mean	1.977(15)	Mean
Cr1–O5(×1)	1.949(18)	2.056(15)	1.899(18)	2.002(15)
Cr1–O6(×1)	2.243(15)		2.171(14)	
Cr1–Cr2(×2)	3.043(15)		3.009(15)	
Cr1–Cr2(×2)	3.182(18)		3.027(18)	
Cr1–Cr3(×2)	2.914(10)		2.967(12)	
Cr2–O1(×1)	2.083(12)		2.052(12)	
Cr2–O2(×1)	1.978(11)		1.988(12)	
Cr2–O3(×1)	1.965(12)	Mean	1.973(13)	Mean
Cr2–O4(×1)	2.006(12)	2.021(12)	1.982(13)	2.002(15)
Cr2–O5(×1)	1.935(13)		1.925(14)	
Cr2–O6(×1)	2.159(11)		2.097(11)	
Cr2–Cr2	2.907(18)		2.806(18)	
Cr2–Cr2	3.193(13)		3.116(13)	
Cr2–Cr3	2.857(14)		2.873(19)	
Cr2–Cr3	2.948(14)		2.922(18)	
Cr2–Cr3	2.929(14)		2.962(17)	
Cr3–O1	2.001(9)		1.964(15)	
Cr3–O2	1.962(13)	Mean	2.022(16)	Mean
Cr3–O2	1.963(13)	2.004(13)	1.946(16)	2.005(16)
Cr3–O3	2.001(13)		2.049(19)	
Cr3–O4	2.048(13)		2.069(17)	
Cr3–O4	2.048(13)		1.983(16)	
Cr3–Cr3	2.524(13)		2.439(20)	
Cr3–Cr3	2.727(13)		2.832(21)	

Cr–Cr intralayer angles (°) (see Fig. 3)

Cr2a–Cr1–Cr3a	59.3(3)
Cr2a–Cr1–Cr2b	57.1(4)
Cr1–Cr2b–Cr3b	58.2(3)
Cr2a–Cr2b–Cr1	61.5(3)

Sum of ionic radii (Å)

Cr^{2+}–O^{2-}(HS)	2.18
Cr^{3+}–O^{2-}	1.995

details. There was some variability in the properties of $SrV_{10}O_{15}$ as seen in Fig. 7 but this was less marked than for the Ba phase. Neutron powder diffraction data for $SrV_{10}O_{15}$ prepared at 1300°C showed no detectable second phase. Although the $BaCr_{10}O_{15}$ sample contained 10.1% Cr_2O_3 as determined from quantitative analysis of the neutron powder data, the properties of this phase are well known. Cr_2O_3 orders in a AFLRO structure below T_N = 308 K and thus it will contribute very little to the susceptibility measured below 300 K (8, 9).

Several comments can be made regarding the data of Figs. 7 and 8. First, the measured susceptibilities at 300 K are lower by factors of 30–50 than values expected for purely paramagnetic systems which indicates the strong influence of antiferromagnetic exchange. Secondly, a Curie–Weiss law region is not observed in the range 300–5 K covered by the measurements which is further evidence for the presence of strong magnetic exchange. Finally, susceptibility maxima are seen at low temperatures for both compounds. For $SrV_{10}O_{15}$, the susceptibility feature is at about 50 K and is quite sharp. A field-cooled–zero-field cooled (FC–ZFC) divergence occurs at essentially the same temperature as the maximum. In contrast the maxima for both $BaCr_{10}O_{15}$ and $BaCr_{10}O_{15+x}$ are very broad, centered at ~25 K, and the FC–ZFC divergence sets in at ~32 K. Sharp maxima are often associated with the onset of AFLRO while broader maxima, along with the FC–ZFC behavior, may indicate spin-glass-type order. There is one further feature, namely, the small upturn at the lowest temperatures in the ZFC curve for both the Cr-based compounds.

Magnetic Neutron Diffraction

$SrV_{10}O_{15}$. Data taken at several temperatures above and below the maximum at 50 K indicate the presence of one fairly weak but sharp, resolution limited, reflection which can be indexed as (111) on the orthorhombic chemical cell and which has a strong temperature dependence. Figure 9 shows this reflection for selected temperatures and in Fig. 10 a more complete temperature dependence of the integrated intensity is recorded which is seen to be

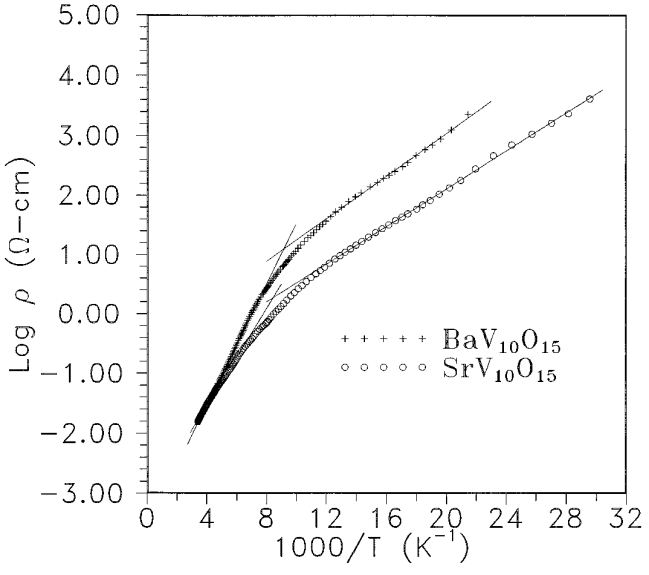

FIG. 6. Resistivity data for $SrV_{10}O_{15}$ and $BaV_{10}O_{15}$. The activation energies are: $SrV_{10}O_{15}$ HT 0.036 eV LT 0.013 eV. $BaV_{10}O_{15}$ HT 0.045 eV LT 0.016 eV.

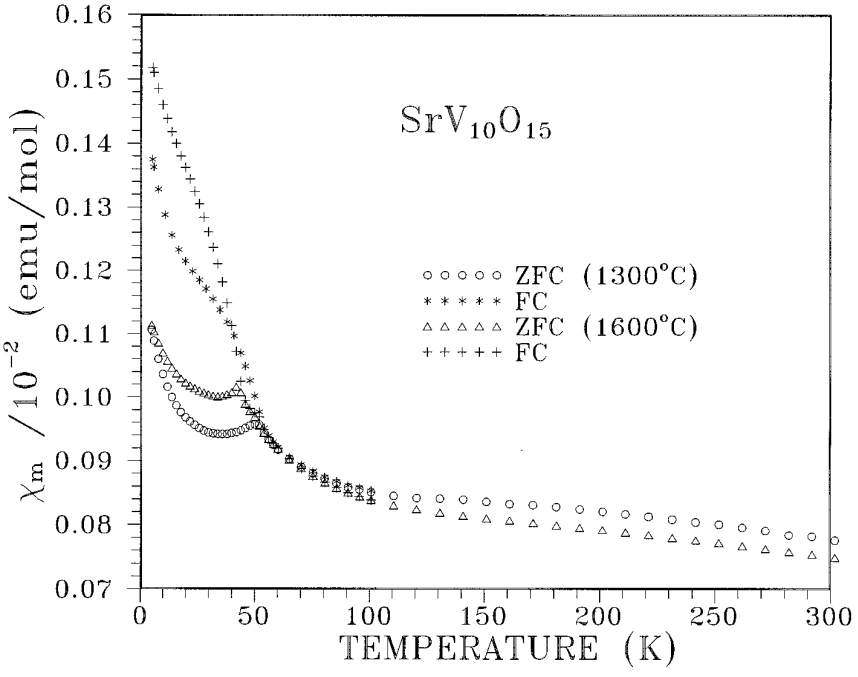

FIG. 7. Susceptibility data for $SrV_{10}O_{15}$.

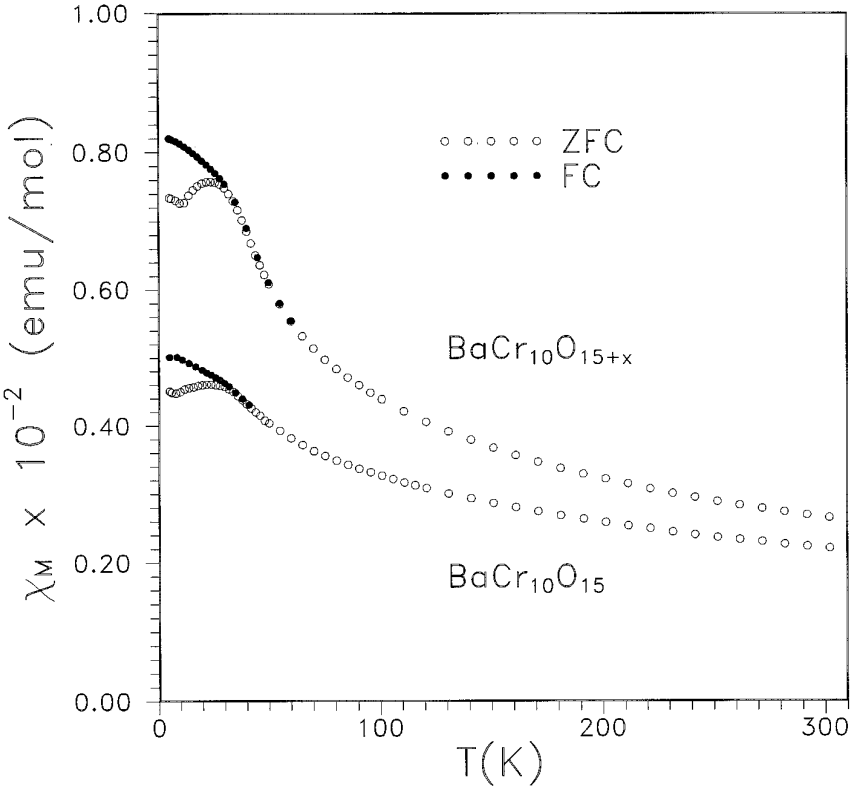

FIG. 8. Susceptibility data for $BaCr_{10}O_{15}$ and $BaCr_{10}O_{15+x}$.

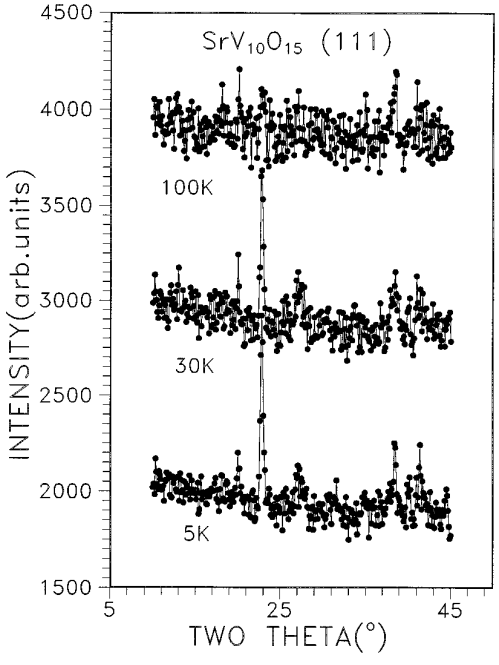

FIG. 9. The (111) reflection for $SrV_{10}O_{15}$ at 5, 30, and 100 K.

consistent with $T_N \sim 50$ K in excellent accord with the susceptibility data. These results are strong evidence for the onset of antiferromagnetic long range order in $SrV_{10}O_{15}$ below 50 K. The essential coincidence in temperature of the susceptibility maximum and the FC–ZFC divergence is probably an indication of the presence of a weak ferromagnetic moment in the AFLRO structure.

Unfortunately, with the observation of only one magnetic reflection it is not possible to deduce a model for the ordered magnetic structure which requires the specification of 40 magnetic moments. For a system in which the V sublattice is characterized by triangular geometries, some type of 120° order is anticipated but better data, perhaps on a single crystal, will be needed to characterize fully the magnetic structure.

$BaCr_{10}O_{15}$. The behavior of this material at low temperatures presents a strong contrast to that of $SrV_{10}O_{15}$. Figure 11 shows data for selected temperatures from 100 K and lower and the key feature is the presence of very broad, diffuse peak centered near $2\theta = 32(°)$ for $\lambda = 2.499$ Å. Data taken at a shorter wavelength $\lambda = 1.392$ Å, and over a wider temperature range, Fig. 12, indicates that this diffuse feature sets in between 180 and 120 K and grows in intensity with decreasing temperature but does not narrow appreciably.

Figure 13 shows a difference plot constructed from $\lambda = 1.392$ Å data, 20–295 K, which isolates the diffuse feature. One relatively prominent Bragg peak is also seen from this plot and can be readily assigned as a magnetic reflection, (012), of the Cr_2O_3 impurity phase. The temperature dependence of the (012) Cr_2O_3 reflection, Fig. 14, is in accord with the published $T_N = 308$ K for this compound. Returning to the diffuse peak it is possible to extract a magnetic correlation length by fitting to a Lorentzian line shape,

$$I(Q) = \frac{A}{Q^2 + 1/\xi^2},$$

where $Q = 4\pi \sin\theta/\lambda$, A is an amplitude, and ξ the correlation length (10). The result of such a fit is shown on Fig. 13 and ξ is 2(1) Å which is on the order the average nearest neighbor Cr–Cr distance in this material, 3.0 Å. It thus appears that antiferromagnetic correlations exist in $BaCr_{10}O_{15}$ which are very short range, extending essentially to nearest neighbors only, and this is consistent with a high level of frustration which can be understood in terms of the topology of the Cr sublattice.

A further remarkable property of this compound can be deduced from the lowest temperature data of Fig. 11. Note that the background at the lowest angles for the 5 K data is significantly greater than for higher temperatures which indicates the presence of small angle scattering (SANS) in $BaCr_{10}O_{15}$. Figure 15 is a difference plot, 5–25 K, which shows this clearly. Magnetic SANS can be ascribed to the presence of short range ferromagnetic order as this is manifest at the reciprocal space origin (000).

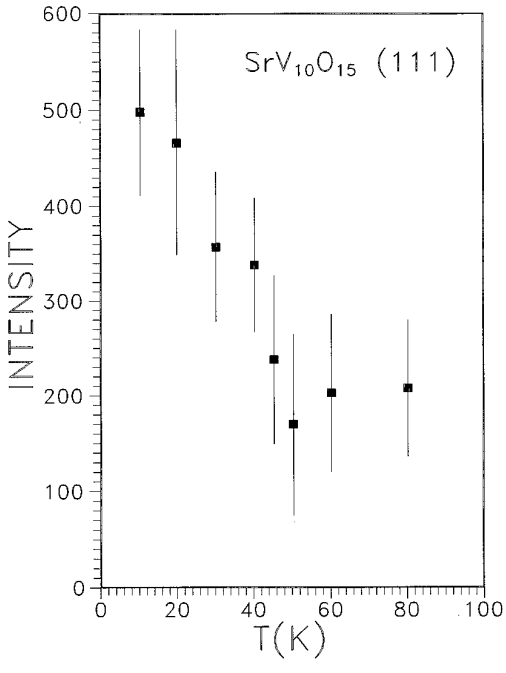

FIG. 10. Temperature dependence of the integrated intensity of the (111) reflection.

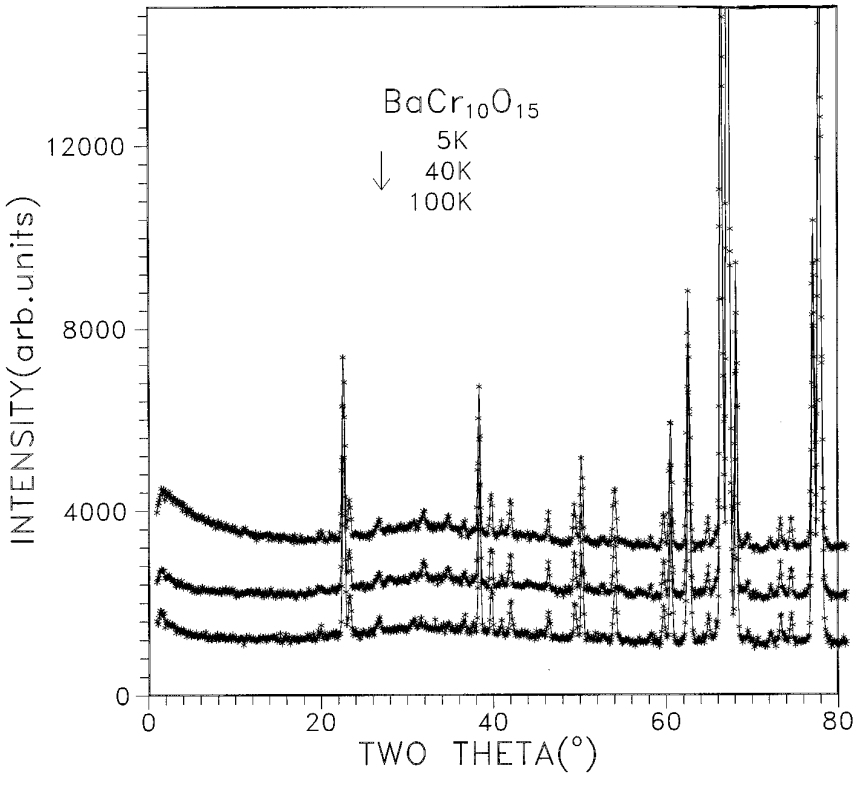

FIG. 11. Neutron diffraction data for $BaCr_{10}O_{15}$ at 100, 40, and 5 K, $\lambda = 2.499$ Å.

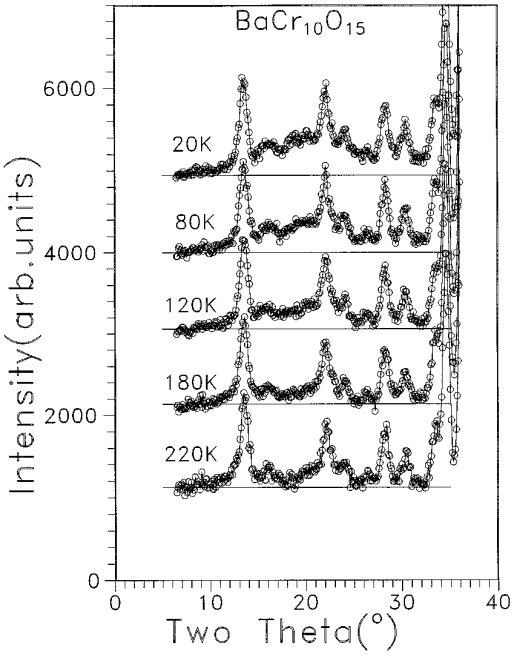

FIG. 12. Neutron diffraction data for $BaCr_{10}O_{15}$ at several temperatures, $\lambda = 1.392$ Å.

Again a correlation length can be extracted by fitting to a Lorentzian and the results plotted as $I(Q)^{-1}$ versus Q^2 are shown in Fig. 16 from which $\xi = 2.9(3)$ Å is obtained. Again, this is on the order of the nearest neighbor Cr–Cr distance. It should be noted that the upturn in the ZFC susceptibility below about 8 K in $BaCr_{10}O_{15}$ is consistent

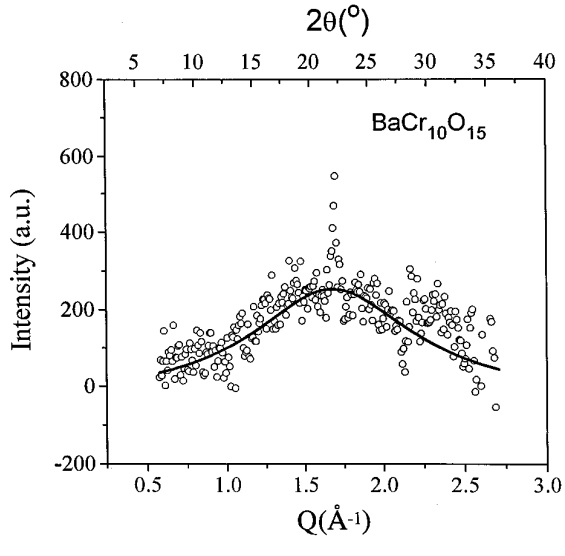

FIG. 13. Difference plot, 20–295 K, for $BaCr_{10}O_{15}$, $\lambda = 1.392$ Å. The solid line is fitted Lorentzian.

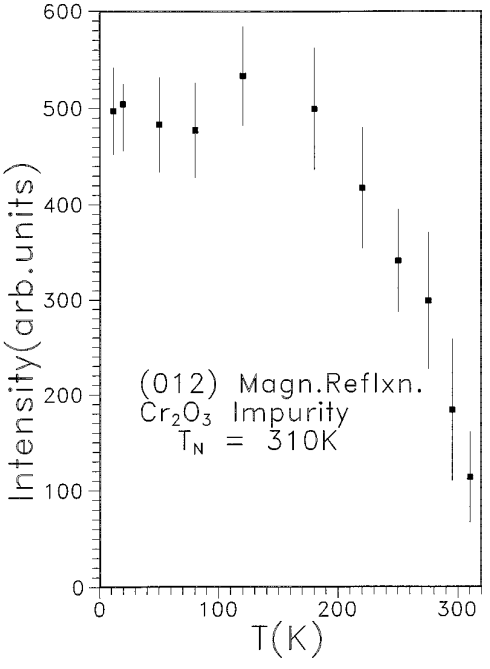

FIG. 14. Temperature dependence of the (012) reflection of Cr_2O_3 showing consistency with $T_N = 308$ K.

with the development of such a short range ferromagnetic component.

$BaCr_{10}O_{15+x}$. As might be expected from the similarity of the bulk susceptibilities, the neutron diffraction results on $BaCr_{10}O_{15+x}$ are quite similar to those for $BaCr_{10}O_{15}$. As Figs. 17 and 18 indicate, a well-developed diffuse reflection is the only temperature dependent feature, apart from the Cr_2O_3 magnetic reflection. One concludes then that only AFSRO is present in this material below 150 K. The upturn in the ZFC susceptibility below about 12 K likely indicates the development of FSRO although SANS data for $BaCr_{10}O_{15+x}$ are lacking.

Comparison to V_2O_3 and Cr_2O_3

Both sets of $AM_{10}O_{15}$ and $AM_{10}O_{15+x}$ materials with M = V or Cr are related structurally to the well-studied binary oxides V_2O_3 and Cr_2O_3. These consist of hcp layers of oxygen atoms with 2/3 instead of 5/8 of the octahedral sites occupied in an ordered manner. Although the site-filling ratio is nearly the same for the two structures, the pattern of occupancy is much more uniform in the sesquioxides where the magnetic atom sublattice consists of layers of edge-sharing, simple (i.e., not centered) hexagons which are slightly puckered. The intralayer metal–metal distances are relatively long, ~3.4–3.6 Å, while the interlayer distances are significantly shorter, 2.6–2.9 Å, due to the stacking sequence which places atoms in the adjacent layers in the center of the hexagonal planes and directly above three alternating corners of the hexagons. Thus, there are no truly frustrated metal–metal interactions either intra- or interplanar. The known magnetic structures of V_2O_3 and Cr_2O_3 show no features which can be traced to frustration (9, 11).

The structural differences just outlined are reflected in the magnetic properties of the two systems. Both V_2O_3 and Cr_2O_3 show AFLRO at relatively high temperatures, 160 and 308 K, respectively. The situation with V_2O_3 is of course quite complex as this material is actually metallic in the corundum structure and undergoes a first order structural transition to the insulating, AFLRO state which has a monoclinic structure below 160 K (11). Cr_2O_3 on the other hand remains insulating and shows no significant structural changes, other than the effects of magnetostriction, near the magnetic ordering temperature of 308 K (8).

The significantly lower transition temperature for $SrV_{10}O_{15}$ relative to V_2O_3 may be traced in part to the influence of the topological frustration inherent in the V sublattice of the former material. The apparently random distribution of V^{2+}/V^{3+} over this sublattice may also play a role.

Cr^{2+}/Cr^{3+} disorder in $BaCr_{10}O_{15}$ is much less significant according to the X-ray and neutron structural results and should be a more minor factor for this material. It is thus all the more remarkable that neither this material nor the oxidized form, $BaCr_{10}O_{15+x}$, which is all Cr^{3+}, show any sign of long range magnetic order down to 5 K. Although

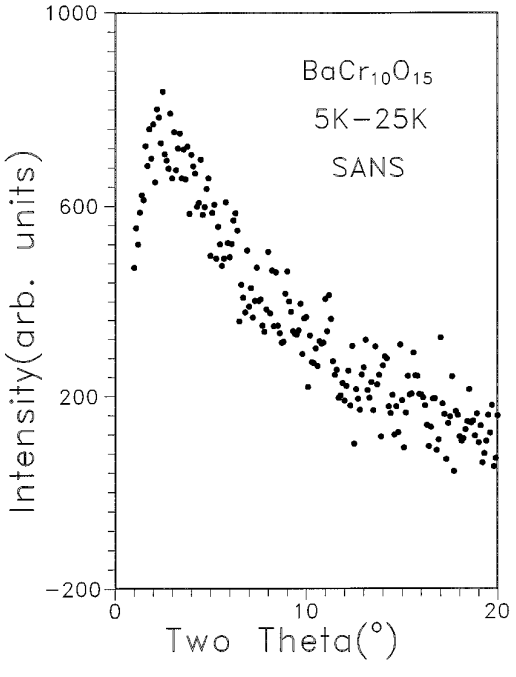

FIG. 15. Difference plot, 5–25 K, for $BaCr_{10}O_{15}$ showing the presence of SANS.

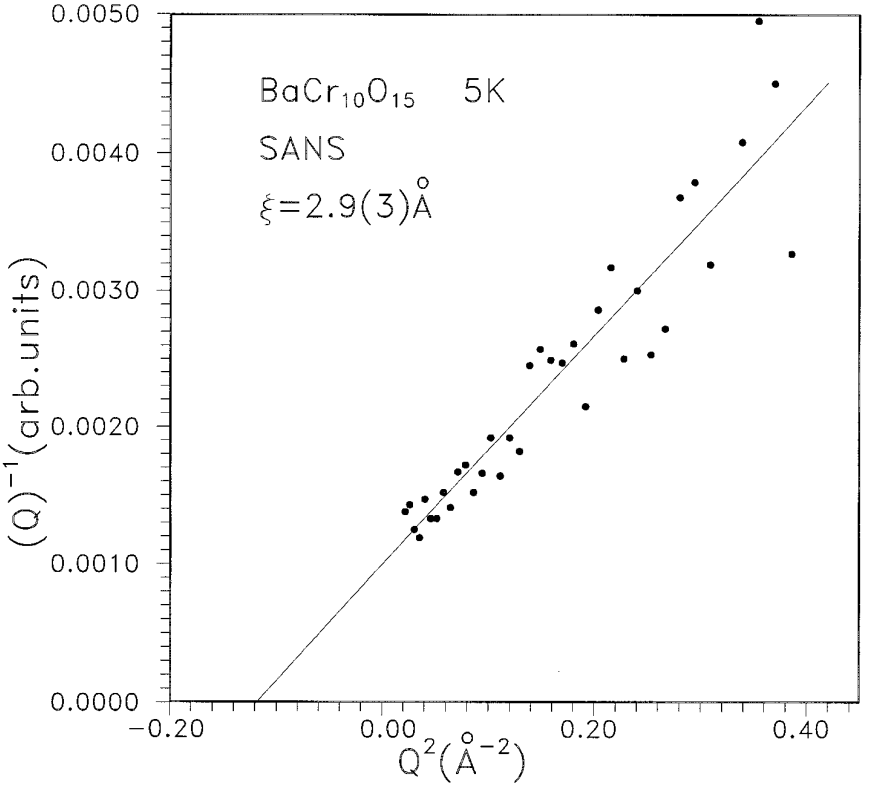

FIG. 16. Plot of $I(Q)^{-1}$ versus Q^2 demonstrating the Lorentzian line shape of the SANS data for $BaCr_{10}O_{15}$.

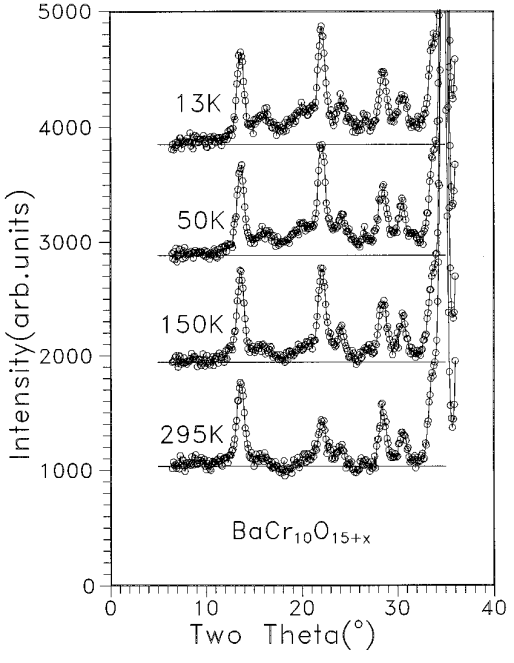

FIG. 17. Diffuse reflection for $BaCr_{10}O_{15+x}$ at various temperatures.

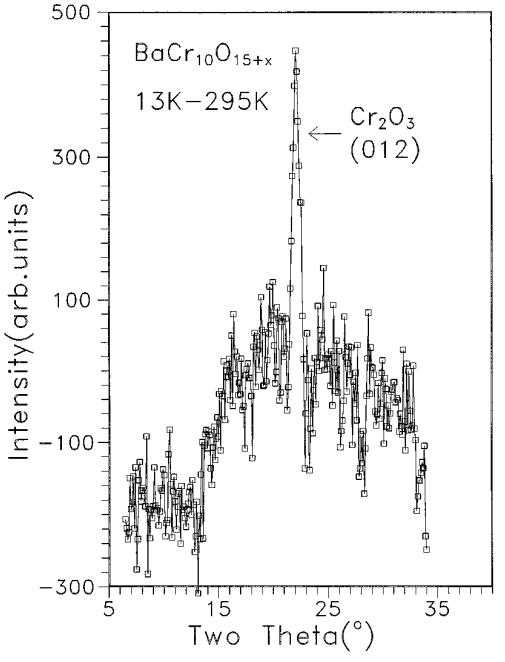

FIG. 18. Difference plot 13–295 K for $BaCr_{10}O_{15+x}$.

several issues, such as the role of disorder on either the Cr or O sublattices remain to be addressed in more detail, there appears to be a strong argument for the role of topological frustration in the inhibition of AFLRO in the Cr—based compounds.

In addition to the above mentioned topics future research on these materials will focus on the complex magnetic and electrical properties of the V-based phases $BaV_{10}O_{15}$, $BaV_{10}O_{15+x}$, and $SrV_{10}O_{15+x}$, procedures to assure better control of stoichiometry, and, ultimately, the preparation of larger single crystals of these remarkable materials.

ACKNOWLEDGMENTS

We thank the Natural Science and Engineering Research Council of Canada for support of this work through a research grant to J. E. Greedan and Infrastructure support of the DUALSPEC facility. R. Donaberger and I. Swainson are acknowledged for assistance with the neutron experiments on DUALSPEC at AECL Research, Chalk River, Canada. McMaster University has provided direct support of the McMaster Nuclear Reactor.

REFERENCES

1. D. Chales de Beaulieu and H. Müller-Buschbaum, *Z. Naturforsch. B* **35,** 669 (1980); *Z. Anorg. Allg. Chem.* **472,** 33 (1981).
2. E. Cuno and H. Müller-Buschbaum, *Z. Anorg. Allg. Chem.* **572,** 89 (1989).
3. Guo Liu and J. E. Greedan, *J. Solid State Chem.* **110,** 274 (1994).
4. J. Rodreguez-Carvajal, "FULLPROF: A program for Rietveld Refinement and Pattern Matching Analysis," Abstracts of the Satellite Meeting on Powder Diffraction of the XV Congress of the International Union of Crystallography, p. 127. Toulouse, France, 1990.
5. D. B. Wiles and R. A. Young, *J. Appl. Crystallogr.* **14,** 149 (1981).
6. G. M. Sheldrick, "SHELX-92, Program for the Refinement of Crystal Structures." University of Göttinger, Germany, 1993.
7. P. W. Selwood, "Magnetochemistry" 2nd ed., p. 78. Interscience, New York, 1956.
8. S. Foner, *J. Appl. Phys. Suppl.* **32,** 635 (1961).
9. B. N. Brockhouse, *J. Chem. Phys.* **21,** 961 (1953).
10. See, for example, H. E. Stanley, "Introduction to Phase Transitions and Critical Phenomena." Oxford Univ. Press, London, 1971.
11. R. M. Moon, *Phys. Rev. Lett.* **25,** 527 (1970); W. B. Yelon, S. A. Werner, S. Shivashankar, and J. M. Honig, *Phys. Rev. B* **24,** 1818 (1981).